Single-neutron excitations in neutron-rich ^{83}Ge and ^{85}Se

J. S. Thomas,[1,*] G. Arbanas,[2] D. W. Bardayan,[3] J. C. Blackmon,[3] J. A. Cizewski,[1] D. J. Dean,[3] R. P. Fitzgerald,[4] U. Greife,[5] C. J. Gross,[3] M. S. Johnson,[1,†] K. L. Jones,[1,‡] R. L. Kozub,[6] J. F. Liang,[3] R. J. Livesay,[5,§] Z. Ma,[7] B. H. Moazen,[6,‡] C. D. Nesaraja,[3,7] D. Shapira,[3] M. S. Smith,[3] and D. W. Visser[4]

[1]*Department of Physics and Astronomy, Rutgers University, New Brunswick, New Jersey 08903, USA*
[2]*Nuclear Science and Technology Division, Oak Ridge National Laboratory, Oak Ridge, Tennessee 37831, USA*
[3]*Physics Division, Oak Ridge National Laboratory, Oak Ridge, Tennessee 37831, USA*
[4]*Department of Physics and Astronomy, University of North Carolina at Chapel Hill, North Carolina 27599, USA*
[5]*Department of Physics, Colorado School of Mines, Golden, Colorado 80401, USA*
[6]*Physics Department, Tennessee Technological University, Cookeville, Tennessee 38505, USA*
[7]*Physics Department, University of Tennessee, Knoxville, Tennessee 37996, USA*

(Received 22 March 2007; published 3 October 2007)

The ^{2}H(^{82}Ge, p)^{83}Ge and ^{2}H(^{84}Se, p)^{85}Se reactions were studied with radioactive beams of ^{82}Ge and ^{84}Se at beam energies of $E_{\text{beam}} = 330$ and 380 MeV, respectively. Excitation energies, proton angular distributions, and asymptotic normalization coefficients have been determined for the lowest lying states of ^{83}Ge and ^{85}Se. Spectroscopic factors have also been extracted under normal assumptions of the bound-state potential properties in the distorted waves Born approximation analysis. However, the peripheral character of the measurements leads to large uncertainties in this extraction. Shell-model calculations have been performed in the region above ^{78}Ni, comparing the single-particle properties of the even-Z, $N = 51$ nuclei up to ^{91}Zr and including ^{83}Ge and ^{85}Se. Direct-semidirect neutron capture calculations to ^{83}Ge and ^{85}Se have also been performed using the spectroscopic input from these (d, p) reaction measurements.

DOI: 10.1103/PhysRevC.76.044302 PACS number(s): 25.60.Je, 21.10.Jx, 26.30.+k, 27.50.+e

I. INTRODUCTION

The interest in the spectroscopy of neutron-rich nuclei near closed shells rests with the important role the single-particle properties of the low-lying states of these nuclei have in our understanding of nuclear structure. Effective nuclear interactions are usually tuned to reproduce experimentally determined energies, spins, and parities of single-particle and single-hole states around the closed nuclear shells. However, although many of these properties are known for nuclei close to stability, there is a decided lack of information for the many nuclei away from stability. In the experimentally less familiar region, there are predictions for changes in the shell structure brought about by the increasing imbalance between proton and neutron number, particularly on the neutron-rich side of stability. The spin-isospin part of the monopole proton-neutron interaction has been shown to cause the migration of single-particle orbitals [1,2], possibly leading to new shell closures in exotic nuclei. Hartree-Fock-Bogoliubov mean-field calculations for diffuse, neutron-rich nuclei also show that, with pairing, these weakly bound systems should exhibit more uniformly spaced single-particle spectra similar to a harmonic oscillator with a spin-orbit interaction [3]. Furthermore, the elemental abundances attributed to the rapid neutron capture (r-) process show patterns that are better explained in calculations that include a mass model with a quenched shell structure [4,5]. In all of these studies, the single-particle excitation energies and strengths help determine the extent of shell structure changes.

In explosive stellar environments, such as that of core-collapsed supernovae, the synthesis of elements in the r-process may be modified by the neutron capture reactions following the fallout from nuclear statistical equilibrium [6]. The r-process is believed to occur at very high temperatures, and the distribution of nuclei is concentrated in the isotopes near closed shells where the binding energy is the largest. As the material cools, neutron captures and β decays of these near-closed-shell nuclei alter the abundance pattern. Neutron capture reactions on neutron-rich, closed-shell nuclei are expected to be dominated by direct capture to bound states, owing to the small Q values for neutron capture and the low level density in the compound nucleus. Direct capture rates on these nuclei depend sensitively on the structure of low-energy states—such as energy levels (neutron separation energies), spins, parities, electromagnetic transition probabilities, and single-particle spectroscopic factors—and typically cannot be accurately estimated in the absence of experimental data [7]. Therefore, there is a clear need for such experimental data near the closed shells to supplement the calculations of direct capture rates.

[*]Present address: School of Electronics and Physical Sciences, University of Surrey, Guildford, GU2 7XH, United Kingdom.
[†]Present address: Lawrence Livermore National Laboratory, Livermore, California 94550, USA.
[‡]Present address: Physics Department, University of Tennessee, Knoxville, Tennessee 37996, USA.
[§]Present address: Nuclear Science and Technology Division, Oak Ridge National Laboratory, Oak Ridge, Tennessee 37831, USA.

II. EXPERIMENTAL TECHNIQUES

The studies of the (d, p) reactions on beams of ^{82}Ge and ^{84}Se were performed at the Holifield Radioactive Ion Beam Facility (HRIBF) at Oak Ridge National Laboratory (ORNL). Both measurements had very similar reaction kinematics, so the detectors were positioned to cover nearly the same angles in the laboratory. Where the two measurements differ is noted. The details of the experimental setup and the results for the ^{83}Ge measurement were first presented in Ref. [8] and are repeated here for completeness.

In the ^{83}Ge measurement, an isobaric $A = 82$ beam at $E_{\text{beam}} = 327$ MeV (4 MeV/nucleon) bombarded a 430 μg/cm^2 CD_2 target for 5 days. A gas-filled ionization chamber was positioned downstream of the target to stop, count, and identify the $A = 82$ beam components using standard energy loss techniques. Figure 1 of Ref. [8] showed the high isobaric contamination of the beam and the necessary clean separation of beam species by atomic number with a resolution of $\Delta Z = 1$. The ^{82}Ge ions of interest comprised 15% of the beam with contamination from stable ^{82}Se (85%) and a trace of ^{82}As (<1%). The average total beam rate over the whole measurement was 7×10^4 pps.

Protons from (d, p) transfer reactions were detected in time coincidence ($\Delta t \approx 80$ ns) with the appropriate beamlike recoil in the ionization chamber. A large-area silicon detector array, SIDAR [9], was positioned to cover the backward laboratory angles $\theta_{\text{lab}} = 105°$–$150°$, corresponding to the center-of-mass (c.m.) angles $\theta_{\text{c.m.}} \simeq 36°$–$11°$. The array consists of six MSL-type YY1 wedges with sixteen annular strips per wedge, manufactured by Micron Semiconductor, Ltd. [10]. The wedges are arranged in a "lampshade" geometry—a six-sided cone where each detector is equally spaced azimuthally and tilted forward 43° from the perpendicular to the beam axis. In this configuration and position, each strip subtended $\Delta\theta_{\text{lab}} \simeq 3°$, and the whole array covers $\Delta\Omega \approx \pi$ steradians in the laboratory.

For the ^{85}Se measurement, an isobaric $A = 84$ beam at $E_{\text{beam}} = 380$ MeV (4.5 MeV/nucleon) impinged upon a 200 μg/cm^2 CD_2 target for nearly 10 days. The higher beam energy and thinner target were chosen to mitigate the degrading effects of beam energy loss on the energy resolution achievable from the measured proton kinematics. The beam was even more contaminated than in the previous experiment. The total beam rate averaged 9×10^4 pps with a composition of 93% ^{84}Br, only 7% ^{84}Se, and traces of other $A = 84$ elements. Figure 1 shows that the $\Delta Z = 1$ separation of the ionization chamber was crucial, as ^{84}Br and ^{84}Se are one unit apart in Z.

Proton-recoil coincidences were established in the same manner as with the ^{83}Ge measurement: The SIDAR in lampshade configuration detected protons at similar backward laboratory angles in time coincidence with a specific beamlike recoil in the ionization chamber. Additionally, in the ^{85}Se measurement, another silicon detector was placed upstream of the lampshade to cover the angular range of $\theta_{\text{lab}} = 160°$–$170°$ ($\theta_{\text{c.m.}} \simeq 10°$–$5°$). This detector, Micron Semiconductor's Design S1 [10], is a flat, annular-strip detector shaped like a compact disk (CD) with inner radius of 24 mm and outer radius of 48 mm. The sixteen annular strips are sectioned into quadrants.

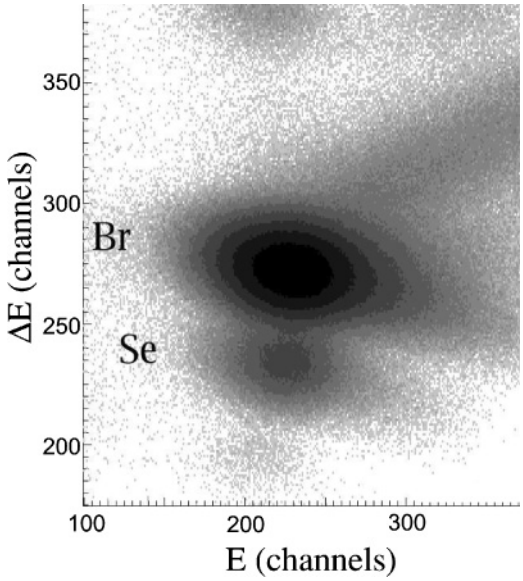

FIG. 1. Energy loss ΔE vs total energy E spectrum for the ionization chamber for the $A = 84$ beam.

III. RESULTS

In both measurements the coincident proton angles and energies were used to identify the states populated in the final nuclei by their excitation energies. The calibration of the proton kinematics for the ^{2}H(^{82}Ge, p)^{83}Ge reaction measurement was accomplished with the proton data from a simultaneous measurement of the ^{2}H(^{82}Se, p)^{83}Se reaction induced by the main beam contaminant. A well-isolated doublet of known states in ^{83}Se ($E_x = 540$ keV and $E_x = 582$ keV [11]), centered at an excitation energy of $E_x \approx 560$ keV, was used to establish the average reaction angle of each strip of SIDAR. The strips were assigned reaction angles such that the measured Se-coincident proton energies corresponding to the population of the doublet states produced the correct excitation energy when transformed to a Q-value spectrum. In this way, the total Q-value spectrum for the ^{2}H(^{82}Se, p)^{83}Se reaction reveals an empirical energy resolution of $\Delta E_x \approx 300$ keV (see Fig. 2 of Ref. [8]).

The Q-value spectrum for the ^{2}H(^{82}Ge, p)^{83}Ge reaction (Fig. 3 of Ref. [8]) was produced with this calibration and analyzed by considering the empirical energy resolution. A large-width group ($\Delta E_x \approx 450$ keV), centered at $Q \approx 1400$ keV, suggests the population of the unresolved ground and first excited states of ^{83}Ge. A fit to the data yields a Q value for the ^{2}H(^{82}Ge, p)^{83}Ge reaction of $Q = 1.47 \pm 0.02$(stat.) $\pm$ 0.07(sys.) MeV and an excitation energy of the first excited state of $E_x = 280 \pm 20$ keV. The remaining excited states of ^{83}Ge are above $E_x \sim 1$ MeV, as seen by the next group of states in the Q-value spectrum centered at $Q \approx 500$ keV.

The excitation energies of a number of low-lying states in ^{85}Se have been determined in a previous measurement of the de-exciting γ rays following the β decay of ^{85}As [12]. The published excitation energies and the recorded proton energies were used to determine the reaction angles covered by SIDAR in the present measurement of the ^{2}H(^{84}Se, p)^{85}Se reaction.

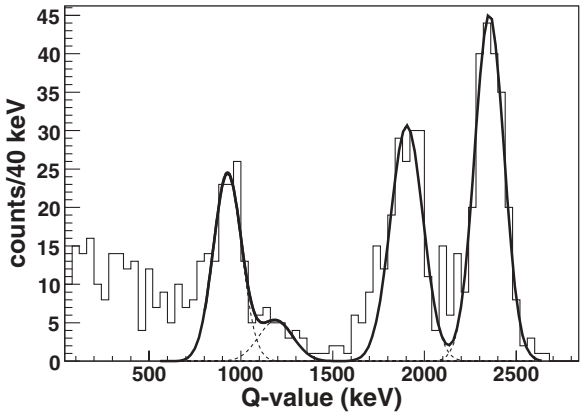

FIG. 2. ^{2}H(^{84}Se, p)^{85}Se Q-value spectrum (all angles). The solid line is a fit for the states of ^{85}Se at the energies taken from Ref. [12], including the ground state, the states at $E_x = 462$ and 1115 keV, and an unresolved doublet ($E_x = 1438 + 1444$ keV).

In particular, the angles of SIDAR strips were determined so that protons from the population of either the ground or first excited state ($E_x = 462$ keV [12]) yielded a correct Q value for the corresponding state (see Fig. 2).

With this method, the excitation energies of all four groups populated in the present measurement were found to be consistent with those measured previously. Figure 2 shows the kinematically reconstructed Q-value spectrum for the ^{2}H(^{84}Se, p)^{85}Se reaction. (Excitation energy in ^{85}Se runs from right to left.) The ground and first excited ($E_x = 462$ keV) states are clearly separated, and the c.m. energy resolution is $\Delta E_{\text{c.m.}} \approx 220$ keV. There is also evidence of the second excited state at $E_x = 1115$ keV ($Q = 1.21$ MeV) and a group centered at $E_x = 1441$ keV ($Q = 0.88$ keV), most likely two unresolved states with $E_x = 1438$ keV and $E_x = 1444$ keV [12].

A. Differential cross sections

Absolute differential cross sections as a function of angle for the observed states were determined from the data through the relationship

$$\frac{d\sigma(\theta_i)}{d\Omega} = \frac{N(\theta_i)}{I\,\Delta\Omega(\theta_i)n} \cdot \frac{\Delta\Omega_i^{\text{lab}}}{\Delta\Omega_i^{\text{c.m.}}}, \qquad (1)$$

where θ_i is the average angle of the ith angular bin; $N(\theta_i)$ is the number of recoil-coincident protons observed in the ith angular bin; I is the integrated beam current measured in the ionization chamber (see Fig. 1); $\Delta\Omega(\theta_i)$ is the laboratory solid angle subtended by the silicon detectors in the ith angular bin; n is the areal density of target deuterons; and $\Delta\Omega_i^{\text{lab}}/\Delta\Omega_i^{\text{c.m.}}$ is the Jacobian of the transformation from the laboratory to c.m. coordinates for the ith angular bin. In both measurements an angular bin consisted of four consecutive annular strips in the lampshade portion of the silicon array. The CD detector was partitioned into two, 8-strip bins. This grouping was done to improve the statistics for each point of the distributions.

The differential cross sections determined from the present measurements were analyzed within the framework of the distorted waves Born approximation (DWBA). Because elastic scattering was not measured in the two reactions, global optical model parameter sets were used in the DWBA analyses. The deuteron parameters of Lohr and Haeberli [13] and the proton parameters of the UNC group [14] were found to be well suited for the data from both reactions. These same parameters also reproduced well the published angular distributions and spectroscopic factors of (d, p) transfer reactions to even-Z, $N = 51$ isotopes from ^{87}Kr to ^{91}Zr [15]. Table I summarizes the optical model parameters used in the DWBA calculations.

First reported in Ref. [8], the c.m. distributions for transfer to the first two states of ^{83}Ge are shown again in Fig. 3. The uncertainties on the data are statistical. The solid curves are fitted distorted waves calculations for the reaction from the TWOFNR code [16] for $\ell = 2$ transfer to the ground state and $\ell = 0$ transfer to the first excited state in ^{83}Ge, both consistent with the empirical angular distributions. The $\ell = 2$ transfer to the ground state of ^{83}Ge supports a level assignment of $J^\pi = 3/2^+$ or $J^\pi = 5/2^+$, but the energy-level systematics of $N = 51$ isotones [18] suggest a $J^\pi = 5/2^+$ assignment, which has been adopted [8]. The $\ell = 0$ first excited state can only be assigned $J^\pi = 1/2^+$. The distorted waves calculations of Fig. 3 were made by assuming the population of the $1d_{5/2}$ neutron orbital for the ground state and the $2s_{1/2}$ orbital for the first excited state (with the convention, e.g., $0s_{1/2}$ for the first s state).

Proton angular distributions from the ^{2}H(^{84}Se, p)^{85}Se reaction have been extracted for the groups in the Q-value spectrum of Fig. 2. The extracted angular distributions for transfer to the ground and first excited states of ^{85}Se are

TABLE I. Global optical model parameters of Lohr and Haeberli [13] (deuteron) and Varner *et al.* [14] (proton), as input into the DWBA code TWOFNR [16]. The reader is referred to the original works for the functional forms of the optical model potentials and their dependencies on energy, atomic number, and atomic mass.

	V[a] (MeV)	r_0 (fm)	a_0 (fm)	W (MeV)	W_D (MeV)	r_W (fm)	a_W (fm)	V_{so} (MeV)	r_{so} (fm)	a_{so} (fm)	r_C (fm)
^{82}Ge+d	107.33	1.05	0.86	0.0	11.55	1.43	0.749	7.0	0.75	0.5	1.3
^{83}Ge+p (g.s.)	56.14	1.195	0.69	0.84	9.59	1.226	0.72	5.9	1.062	0.65	1.268
^{84}Se+d	108.21	1.05	0.86	0.0	11.37	1.43	0.749	7.0	0.75	0.5	1.3
^{85}Se+p (g.s.)	55.31	1.195	0.69	0.92	9.14	1.227	0.72	5.9	1.062	0.65	1.268
n	[b]	1.25	0.65	0.0	0.0	–	–	6.0	1.25	0.65	1.25

[a]The parameter definitions here follow the normal conventions and correspond to those found in Ref. [17].
[b]Fit to reproduce the binding energy of the neutron.

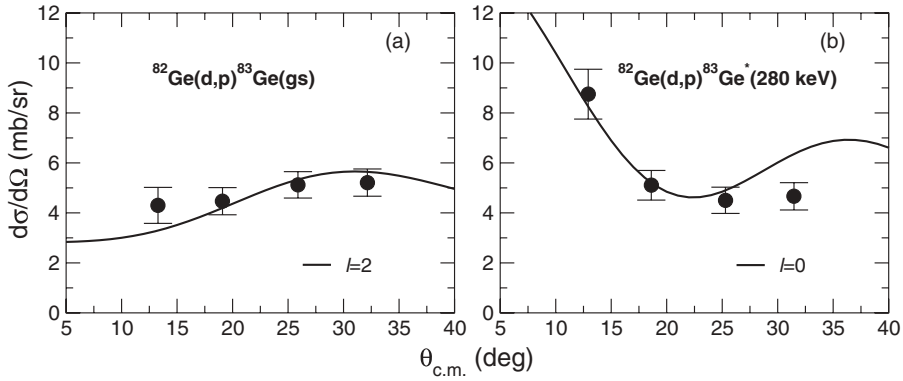

FIG. 3. Proton angular distributions as functions of c.m. angle for ^{83}Ge. (a) Ground-state fit by $\ell = 2$; (b) $E_x =$ 280 keV fit by $\ell = 0$.

presented in Fig. 4; the uncertainties are purely statistical. Distorted waves calculations, shown as solid lines in Fig. 4, were made with the TWOFNR code by using the globally parameterized potentials, summarized in Table I, adjusted for the ^{2}H(^{84}Se, p)^{85}Se reaction at $E_{\text{beam}} = 4.5$ MeV/nucleon. Neutron configurations of $1d_{5/2}$ (ground state) and $2s_{1/2}$ (first excited state) were assumed for the calculations. Based on the same arguments as for the transfer to ^{83}Ge, the level assignments of $J^\pi = 5/2^+$ for the ground state of ^{85}Se and $J^\pi = 1/2^+$ for the first-excited state at $E_x = 462$ keV have been adopted, supporting the assignments in Ref. [12].

The data for the higher lying excitations of ^{85}Se have also been analyzed. Information from the CD detector was not included because the proton energies associated with these excitations are lower than the energy threshold of the detector.

The previous work of Omtvedt *et al.* suggested the tentative assignment of $J^\pi = (3/2^+, 7/2^+)$ for the state at $E_x =$ 1.115 MeV [12]. The tentative assignment could indicate the population of either the neutron $1d_{3/2}(\ell = 2)$ or $0g_{7/2}(\ell = 4)$ configuration in ^{85}Se. The empirical proton angular distribution and DWBA calculations for $\ell = 2$ and $\ell = 4$ transfers are presented in Fig. 5. The low cross section populating the $E_x = 1.115$ MeV state ($Q \approx 1.21$ MeV in Fig. 2) either suggests very weak $2d_{3/2}$, $\ell = 2$ strength for a $3/2^+$ state or is a consequence of the poor angular momentum matching that inhibits $\ell = 4$ transfers (to the $0g_{7/2}$ configuration) in (d, p) reactions [19]. There appears to be a slight preference for the fit with the $\ell = 4$ calculation; however, the uncertainty of each fit is nearly 20%, precluding either assignment.

For completeness, the proton distribution from transfer to a doublet of states centered at $E_x = 1.441$ MeV ($E_x =$ 1.444 MeV and $E_x = 1.438$ MeV) is shown in Fig. 5. The DWBA calculations in Fig. 5 are not fits to the data; rather, they are representative of $\ell = 2$, $d_{3/2}$ and $d_{5/2}$ transfer, showing the insensitivity to total angular momentum transfer. No simple, single-ℓ transfer can explain the shape of this distribution. The shape of an $\ell = 0$ transfer would peak at $\theta_{\text{c.m.}} = 0^\circ$ and again at $\theta_{\text{c.m.}} = 35^\circ$; an $\ell = 1$ transfer would peak before the $\ell = 2$ transfers shown in Fig. 5, but that would imply the population of a negative-parity state in the neutron *sdg* shell; and any transfer greater than $\ell = 2$ would not peak forward of $\theta_{\text{c.m.}} = 35^\circ$.

B. Spectroscopic factors and ANCs

The normal prescription to extract a spectroscopic factor from transfer data is to normalize a DWBA calculation to the measured differential cross section. This has been done for the populated states in ^{85}Se and ^{83}Ge. The spectroscopic information derived from the two measurements of this study is summarized in Table II and includes the previously reported results for ^{83}Ge [8]. The 30% uncertainties on each spectroscopic factor are the combination in quadrature of a

TABLE II. Summary of spectroscopic quantities determined from the measurements of the ^{82}Ge,^{84}Se(d, p) reactions in the present work. The ℓ are the transferred orbital angular momenta, J^π are the assigned (tentative) spins and parities, $S_{\ell j}$ are the extracted spectroscopic factors, C^2 are the squared ANCs, and $S_{\ell j}^{\text{scaled}}$ are the rescaled spectroscopic factors used in the direct capture calculation (see text). Spectroscopic factors and ANCs for both ℓ transfers are given for the 1.115-MeV excitation in ^{85}Se. The excitation energies of the states of ^{85}Se are taken from Ref. [12].

$^A X$	E_x (MeV)	ℓ	J^π	$S_{\ell j}$	$C^2_{\ell j}$ (fm^{-1})	$S_{\ell j}^{\text{scaled}}$
^{83}Ge	0.0	2	$5/2^+$	0.48 ± 0.14	3.99 ± 0.94	0.53
	0.28 ± 0.02	0	$1/2^+$	0.50 ± 0.15	25.2 ± 5.9	0.52
^{85}Se	0.0	2	$5/2^+$	0.33 ± 0.10	6.11 ± 1.43	0.38
	0.462	2	$1/2^+$	0.30 ± 0.09	25.3 ± 5.9	0.32
	1.115	(2)	$(3/2^+)$	(0.06 ± 0.02)	(0.42 ± 0.11)	–
		(4)	$(7/2^+)$	(0.77 ± 0.27)	(0.049 ± 0.012)	–
	$1.438 + 1.444$	–	–	–	–	

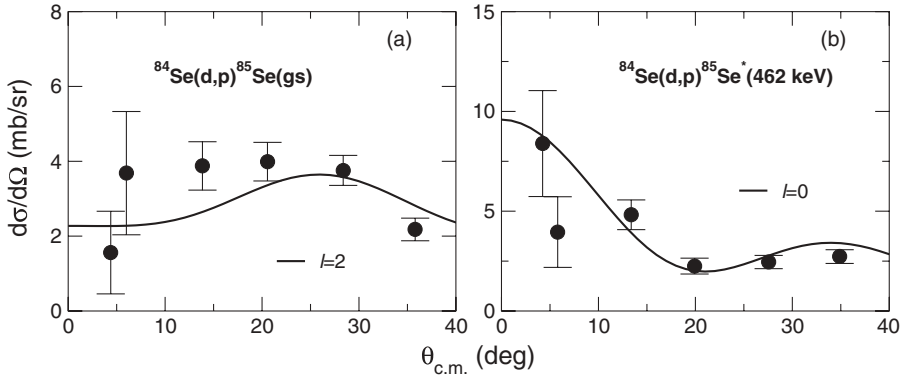

FIG. 4. Proton angular distributions as functions of c.m. angle for ^{85}Se. (a) Ground state fit by $\ell = 2$; (b) $E_x =$ 462 keV fit by $\ell = 0$.

6% statistical best-fit uncertainty in the fitting to the measured differential cross section, an estimated 15% uncertainty in the determination of the target thickness (affecting the absolute normalization), an estimated 17% uncertainty from the choice of optical model parameters, and an estimated 19% systematic uncertainty from the ambiguity of the geometrical parameters in the bound-state potential of the DWBA calculation.

It is this last uncertainty that, in general, leads to the largest overall uncertainties associated with an extracted spectroscopic factor, typically 20%–30%. The calculated distribution for the reaction $A(d, p)B$ depends on an overlap function, $I(r) = \langle A + n|B\rangle$, a many-body quantity that is usually approximated by a single-particle bound-state wave function [19]. The bound-state geometrical parameters determining the single-particle wave function for the DWBA calculation are essentially arbitrary; the parameters used reflect a choice in the model of the wave function and should be quoted along with the extracted spectroscopic factor [19]. The uncertainties associated with this ambiguity for the data in Table II were estimated by varying the bound-state potential radius parameter, r, in the DWBA calculation between 1.2 to 1.3 fm and examining the effect on the extracted spectroscopic factors. All of the values in the table assume a central value $r = 1.25$ fm.

Several authors [19–23] have noted that the angular distributions calculated within the DWBA framework, and used to extract spectroscopic factors, can be rather insensitive to the parts of the overlap functions in the nuclear interior, $r < R_N$, particularly for reactions at or below the Coulomb barrier. It has also been shown that this insensitivity to the nuclear interior can be extended to reactions above the Coulomb barrier, provided the reaction is still peripheral or occurs at, or outside, the nuclear surface [24].

Figure 6 shows DWBA calculations for (d, p) transfer to the ground and first excited states of ^{83}Ge at a beam energy of $E_{\text{beam}} = 4$ MeV/nucleon. The calculations differ in the lower cutoff radius applied to all radial integrals. For a cutoff radius out to ∼8 fm, the magnitude and shape of the most forward, prominent peak changes by less than 10%. The relative insensitivity to the nuclear interior parts of the integrals suggests that it is the *tail* of the overlap function that determines the magnitude of the DWBA calculation and that a differential cross section from a peripheral transfer reaction is a better measure of the *asymptotic normalization coefficient* (ANC) of the overlap function, rather than the spectroscopic factor [24].

The overlap function in the nuclear exterior must decay exponentially if it is to describe properly the condition of a bound state. In the case of an uncharged bound particle (e.g., a neutron), the exponential decay is governed by the tail of a spherical Hankel function with the magnitude (the ANC) determined by measurement [19,24]. The single-particle wave functions that are traditionally used to approximate the overlap functions must also behave in the same exponentially decaying manner. Each single-particle wave function must also be normalized. Together, these two conditions fix a single-particle ANC for each assumed bound-state potential geometry. The ANC ($C_{\ell j}$), single-particle ANC ($b_{\ell j}$), and spectroscopic factor ($S_{\ell j}$) are related by the equation [24]

$$C_{\ell j}^2 = S_{\ell j} b_{\ell j}^2. \tag{2}$$

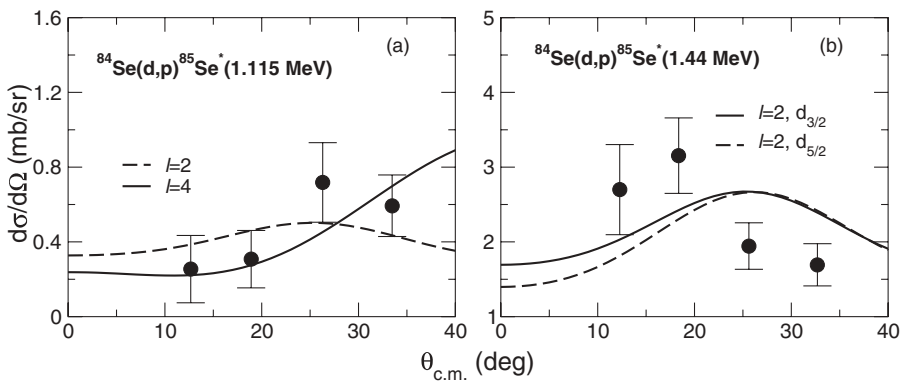

FIG. 5. Proton angular distributions as functions of c.m. angle for higher lying excitations in ^{85}Se. (a) $E_x = 1.115$ MeV and fit with $\ell = 2$ and $\ell = 4$ DWBA calculations; (b) $E_x = 1.438 + 1.444$ MeV data and $\ell = 2$.

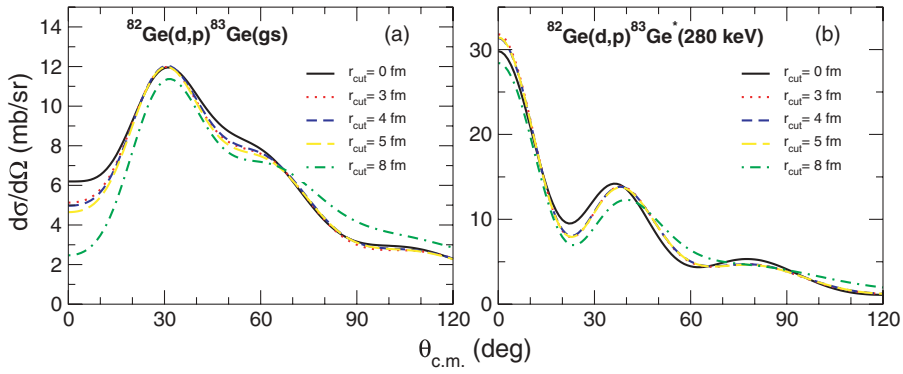

FIG. 6. (Color online) DWBA calculated angular distributions for ^{83}Ge with varying radial cutoffs in the overlap functions. (a) Ground state; (b) $E_x = 280$ keV state.

The normalization of the asymptotic part of the overlap function, determining the magnitude of the differential cross section for the peripheral transfer reaction, is divided into a model-dependent quantity, $b_{\ell j}$, and an equally model-dependent extracted spectroscopic factor, $S_{\ell j}$. However, if the measured reaction is peripheral, the magnitude of the tail of the overlap function is more directly determined, and the model-dependent quantities of single-particle ANC, $b_{\ell j}$, and extracted spectroscopic factor, $S_{\ell j}$, combine as in Eq. (2) to give a model-independent ANC, $C_{\ell j}$. As suggested in Ref. [24], the $C_{\ell j}$ can be used more reliably than a spectroscopic factor in subsequent studies of reactions related to the one measured, such as the direct radiative capture of a nucleon involving the same initial and final nuclei.

In both of the measurements of the present study, the beam energies placed the reactions approximately 1 MeV above the respective Coulomb barriers, suggesting the reactions should have a strong peripheral character. Figure 7 shows the dependencies of the extracted spectroscopic factors and ANCs on the single-particle ANCs for the first two states of ^{83}Ge. Figure 8 is the corresponding figure for the first two states of ^{85}Se. The single-particle ANCs, $b_{\ell j}$, are varied by changing the bound-state potential geometry through the radius and diffuseness of a Woods-Saxon shape, as suggested in the method described in Ref. [25]. In each case, the extracted spectroscopic factor changes by large factors (up to 2 or 3) whereas the squared ANC, $C^2_{\ell j}$, changes by a few percent. The values determined for the $C_{\ell j}$ are nearly model independent, demonstrating the largely peripheral natures of the studied transfer reactions.

There remains a small dependency of the extracted squared ANC, $C^2_{\ell j}$, on the single-particle ANC, $b_{\ell j}$, for the studied cases of $\ell = 0$ transfers. In comparing the most forward peaks of Figs. 6(a) and 6(b), it is seen that the remaining dependency may have been expected, considering the larger influence of the nuclear interior on the DWBA calculation for the $\ell = 0$ transfers. However, there is a small effect ($\sim$1%) of just adopting the average value of the $C^2_{\ell j}$ in these cases. The squared ANCs, $C^2_{\ell j}$, are subject to the same uncertainties as the extracted spectroscopic factors less the uncertainty from the ambiguity of the bound-state potential parameters of the DWBA calculations.

Table II lists the $C^2_{\ell j}$ values determined for the states observed in the two measurements of the present study, along with the now reduced uncertainties (as percentages of the whole) associated with these quantities. For the $E_x = 1.115$ MeV state, values in parentheses represent the ANC value found by assuming the listed level assignment options.

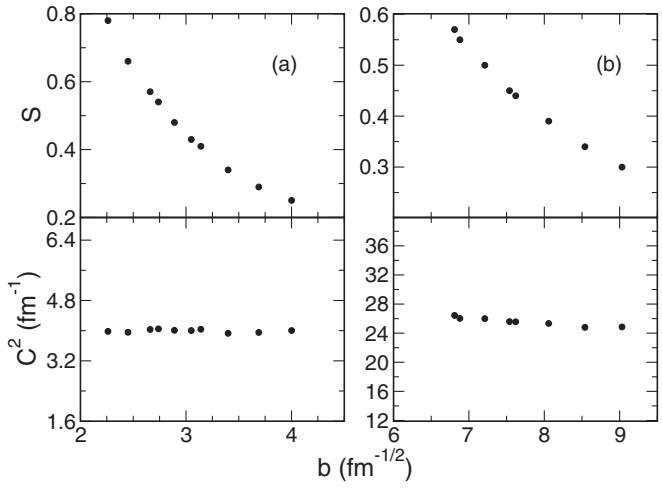

FIG. 7. Dependencies of the extracted spectroscopic factors, S, and asymptotic normalization coefficients, C^2, on the single-particle ANCs, b, for ^{83}Ge. The single-particle ANCs are themselves functions of the bound-state potential geometry. (a) Ground state; (b) $E_x = 280$ keV state.

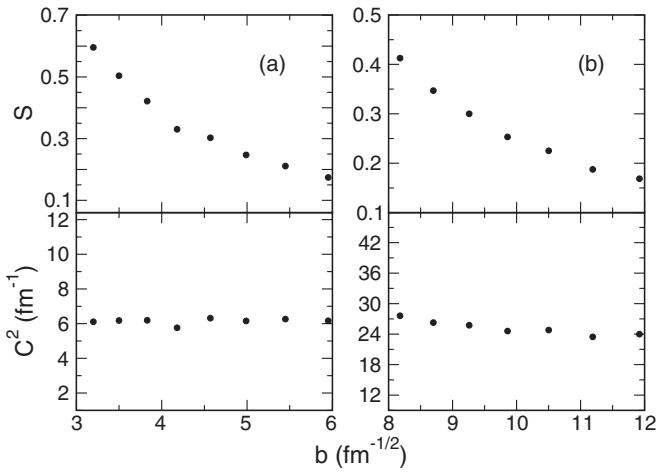

FIG. 8. Dependencies of the extracted spectroscopic factors, S, and asymptotic normalization coefficients, C^2, on the single-particle ANCs, b, for the (a) ground state and (b) $E_x = 462$ keV state in ^{85}Se.

IV. DISCUSSION

A. Shell-model calculations

The experimental results are compared to shell-model calculations in the region. An effective two-body interaction in the model space is obtained by starting from the free nucleon-nucleon interaction V that is appropriate for descriptions of nuclear physics at low and intermediate energies, the charge-dependent version of the Bonn potential models [26]. This and other modern nucleon-nucleon interactions typically have a strongly repulsive core that is renormalized by building a reaction G matrix. In diagrammatic language the G matrix represents the sum over all ladder diagrams. The G matrix is incomplete in the sense that it only sums to all orders the particle-particle ladder diagrams. Long-range effects represented by core-polarization terms are also included, by renormalizing the G-matrix elements by the $\hat{Q}$-box method. Nonfolded, irreducible, and valence linked diagrams make up the $\hat{Q}$ box. All nonfolded diagrams to third order in G are included [27]. An effective interaction $\tilde{H}$ is then computed in terms of the $\hat{Q}$ box by using the folded-diagram expansion method; see Ref. [27] for further details.

The model space consists of the $0f_{5/2}$-$1p$-$0g_{9/2}$ proton and $0g_{7/2}$-$1d$-$2s$-$0h_{11/2}$ neutron spaces, where the core is taken as ^{78}Ni with a closed $0f_{7/2}$ proton orbital and a closed neutron shell at $N = 50$. The interaction is defined by both the single-particle energies within the model space and the effective two-body interaction in that space. The single-particle energies for Set-A are taken from Ref. [28] and are summarized in Table III. To explore the effect of the placement of the $0g_{9/2}$ orbital on the structure, a Set-B was used where this single-particle energy was changed to $\varepsilon(0g_{9/2}) = 4.5$ MeV.

This effective two-body interaction was used in shell-model calculations. The shell-model problem is an eigenvalue problem, requiring the solution to $\tilde{H}|\Psi_k\rangle = E_k|\Psi_k\rangle$, with $k = 1, \ldots, K$. The Lanczos algorithm was employed to find the lowest (and highest) eigenvalues and eigenvectors (up to typically $K = 10$). The basic algorithm was first proposed in Ref. [29]. Calculations were performed using the Strasbourg shell-model code ANTOINE [30,31].

Using this interaction gives a $5/2^+$ state that is always the lowest for the $N = 51$ systems. The splitting between the $5/2^+$ and $1/2^+$ states, shown in Fig. 9 with the experimental values, is calculated with Set-A to be 0.474, 0.446, 0.744, 1.07, and 1.02 MeV for ^{83}Ge, ^{85}Se, ^{87}Kr, ^{89}Sr, and ^{91}Zr, respectively. The corresponding energy differences in the calculations with Set-B are 0.417, 0.361, 0.674, 1.24, and 1.66 MeV. Although this is not in perfect agreement with experiment, it does give the correct trend, with ^{89}Sr and ^{91}Zr showing a larger splitting between the two energy levels than is found in ^{83}Ge and ^{85}Se. The excitation energies of the first 2^+ states in the even-even, $N = 50$ isotones were also calculated, and these are shown compared to the experimentally determined values in Fig. 9.

TABLE III. Proton and neutron single-particle energies, ε, used in the shell-model calculations, taken from Ref. [28]. Set-A differs from Set-B only in the placement of the proton $0g_{9/2}$ orbital.

Proton orbital	ε (MeV)	Neutron orbital	ε (MeV)
$0f_{5/2}$	0.0	$1d_{5/2}$	0.0
$1p_{3/2}$	1.1	$2s_{1/2}$	1.3
$1p_{1/2}$	2.5	$0g_{7/2}$	1.8
$0g_{9/2}$ Set-A	3.3	$1d_{3/2}$	2.4
$0g_{9/2}$ Set-B	4.5	$0h_{11/2}$	3.0

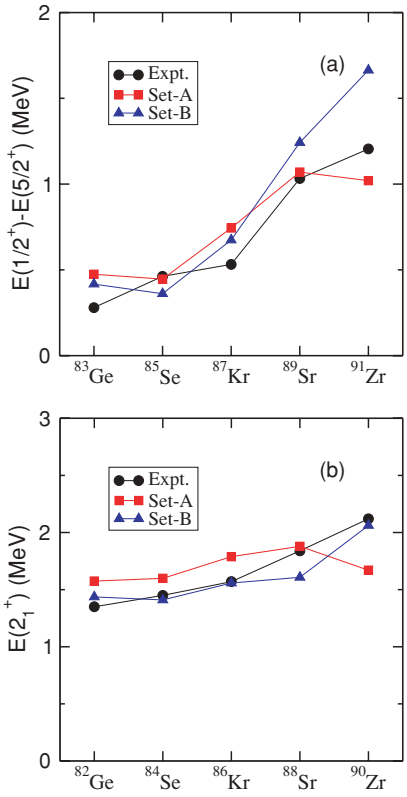

FIG. 9. (Color online) (a) Energy differences between the first $1/2^+$ and $5/2^+$ states in the $N = 51$ isotones. Experimental values for ^{83}Ge are taken from the present measurement, those for ^{85}Se from Ref. [12], and the others from Ref. [18]. (b) Excitation energies of the first 2^+ states in the even-even, $N = 50$ isotones, calculated with both potential sets and compared to experimental values (taken from Ref. [18]).

The calculated spectroscopic factors, which are given by $S(j) = |\langle\Psi_f(J_f)|a_j^\dagger|\Psi_i(J_i)\rangle|^2$, are shown in Table IV. Here, J_i is the initial-state total angular momentum (the $N = 50$, 0^+

TABLE IV. Calculated and extracted spectroscopic factors, $S(j)$, as defined in the text, for the first $5/2^+$ and $1/2^+$ levels in the $N = 51$ isotones. The spectroscopic factors for ^{87}Kr [32], ^{89}Sr [33], and ^{91}Zr [34] are assumed to have ~25% uncertainties.

^{A}X	Exp.		Set-A		Set-B	
	$5/2^+$	$1/2^+$	$5/2^+$	$1/2^+$	$5/2^+$	$1/2^+$
^{83}Ge	0.48 ± 0.14	0.50 ± 0.15	0.73	0.38	0.71	0.35
^{85}Se	0.33 ± 0.10	0.30 ± 0.09	0.73	0.36	0.71	0.32
^{87}Kr	0.56	0.46	0.79	0.46	0.78	0.40
^{89}Sr	1.06	1.03	0.83	0.62	0.85	0.71
^{91}Zr	1.09	0.88	0.80	0.55	0.97	0.90

states) and J_f is the final-state angular momentum (either 5/2 or 1/2), and j corresponds to the addition of the extra neutron in one of the five neutron orbitals. The spectroscopic factors for the reactions ^{86}Kr$(d, p)^{87}$Kr [32], ^{88}Sr$(d, p)^{89}$Sr [33], and ^{90}Zr$(d, p)^{91}$Zr [34] are shown in Table IV. The uncertainties in these spectroscopic factors are not given in the original studies, but they are assumed to be ∼25%, typical of a DWBA analysis.

The Set-A values for the spectroscopic factors are only in qualitative agreement with experiment; better general agreement is obtained with Set-B. The placement of the $0g_{9/2}$ orbital to a higher energy appears to be mainly responsible for keeping the nucleus from becoming deformed at ^{90}Zr and in generating a more robust spectroscopic factor. Also note that, in both Set-A and Set-B, the spectroscopic factor for the $1/2^+$ state is less than that for the $5/2^+$-ground state, as is also the trend experimentally.

The present calculations fail to reproduce the low excitation energy of the $1/2^+$ state in ^{83}Ge. This could be because correlations that come from the $0f_{7/2}$ orbital within our model space were not included, and it may indicate a need to open the $0f_{7/2}$ orbital in the protons to include further configuration mixing.

The calculated occupations for the proton levels in the $N = 50$ and $N = 51$ nuclei from Ga to Zr are summarized in Fig. 10. Using Set-A single-particle energies shows that the $0g_{9/2}$ protons play only a small role until $Z = 40$, where they become a more important component of the structure. Since the $0g_{9/2}$ orbital is deformation-driving, the calculated 2^+ energy decreases, with subsequent increased fragmentation of the single-particle strength. The adjusted $0g_{9/2}$ orbital energy in Set-B does not show this dramatic occupation increase at ^{90}Zr, and, in fact, the $1p_{1/2}$ orbital becomes more fully occupied. For both Set-A and Set-B, the additional neutron yields a shift of particle number out of the $0f_{5/2}$ and into other orbitals.

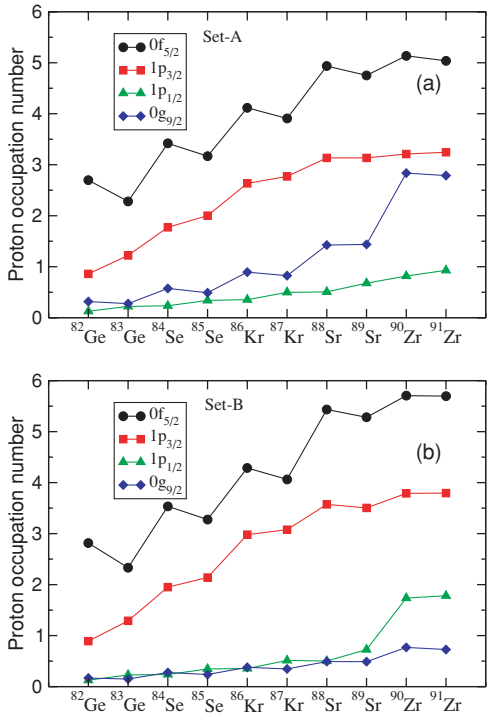

FIG. 10. (Color online) Calculated occupations of the proton levels for odd-A ($N = 51$) and even-even ($N = 50$) isotopes from Ge to Zr for (a) single-particle energy Set-A and (b) Set-B.

B. Direct neutron capture calculations

In the astrophysical scenario of the r-process, the (n, γ) reaction rates on neutron-rich, $N = 50$ isotones may modify the final abundances observed in the $A \sim 80$ peak. The spins and positive parities of the first two states of ^{83}Ge and ^{85}Se mean that the dominant direct capture contributions are expected to be through either s-wave or d-wave neutron capture with a magnetic dipole ($M1$) transition or p-wave neutron capture with an electric dipole ($E1$) transition.

A direct-semidirect (DSD) contribution to the neutron capture cross section was computed with the code CUPIDO [35]. Since the shell effects of heavy targets on direct capture cannot yet be accounted for by the existing unification schemes of shell models and nuclear reactions [36–38], the effect of a target nucleus in the resolved resonance region is conventionally approximated by a real potential well. For the potential well the real part of the Koning-Delaroche global optical potential [39] was used after converting to a Woods-Saxon parametrization. The effect of the giant dipole resonance (GDR)—the semidirect contribution—is treated as a correction to the single-particle electromagnetic (EM) operator [40,41], with the GDR parameters taken from RIPL [42]. The depth of the potential for the capturing single-particle state was adjusted to reproduce the measured binding energy of that state; however, it was found that the potential used for scattering states also reproduced the binding energies of the capturing bound states, with only minor adjustments to the potential depth needed.

The total direct capture cross section is the sum of the cross sections to individual states, weighted by the spectroscopic factors of those states. However, as described in Sec. III B, the spectroscopic factor as usually extracted from differential cross sections of transfer reactions suffers from uncertainties in the bound-state potential. Care must be taken that the spectroscopic factors used in the capture calculations are consistent with the $C_{\ell j}$ determined from the transfer measurement, giving the correct asymptotics of the bound-state wave function.

The single-particle wave functions, $\psi_{\ell j}$, used in the capture calculations are calculated with a model that differs from the wave functions for the DWBA analysis. The geometry of the potential and, most importantly, the asymptotic normalizations of the two sets of wave functions (given by the single-particle ANC, $b_{\ell j}$) are different. The single-particle ANCs, $b_{\ell j}$, are found by determining the asymptotic ratios of the wave functions and the respective spherical Hankel functions, $b_{\ell j} = \psi_{\ell j}/[-i^{\ell} k \cdot h_{\ell}(ikr)]$. The spectroscopic factors that are used in the direct capture calculation are rescaled to reflect this change in the single-particle ANC, $b_{\ell j}$, but remain consistent with the measured ANC, $C_{\ell j}$, through the relationship of Eq. (2). The rescaled spectroscopic factors obtained in this way are found to be 0.53, 0.52, 0.38, and 0.32 for the first four

rows in Table II, close to the values extracted from the transfer measurement.

Electric dipole ($E1$) capture was found to dominate the DSD capture on ^{82}Ge and ^{84}Se. Incoming p-wave neutrons are captured via an $E1$ transition into the lowest $2s$ and $1d$ single-particle states of ^{83}Ge and ^{85}Se. A semidirect capture via the GDR [35] was found to interfere destructively with the direct capture, so that the direct-semidirect capture was smaller than the direct capture alone by ∼10% for both ^{82}Ge and ^{84}Se, as summarized in Fig. 11. The largest $M1$ contribution to the direct capture cross section is smaller by approximately eight orders of magnitude relative to the $E1$ contribution in this single-particle model. The $M1$ matrix element in the long-wavelength approximation is proportional to the overlap of the initial scattering and final bound-state wave functions [43]. Therefore, for two of the allowed transitions—s-wave capture to the bound $2s_{1/2}$ state and d-wave capture of a $d_{5/2}$ neutron to the bound $1d_{5/2}$ state—the $M1$ matrix elements

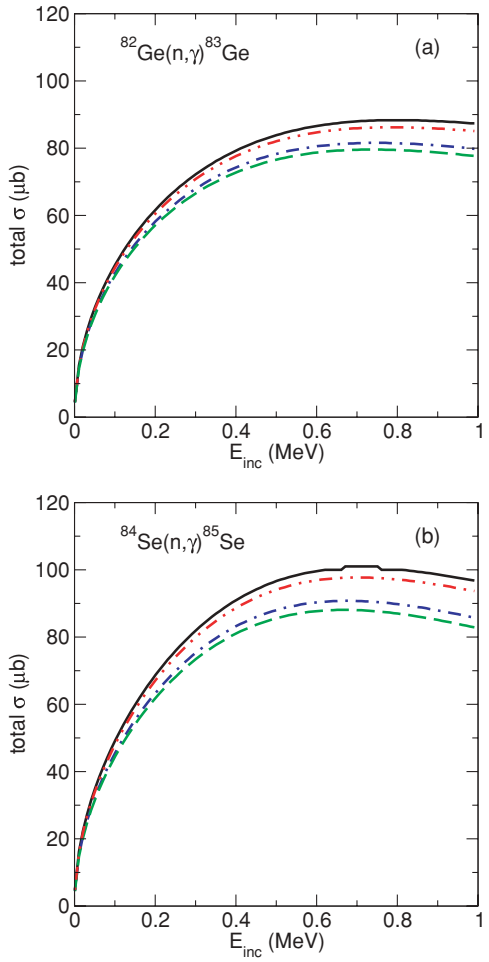

FIG. 11. (Color online) Calculated total capture cross sections for the reactions (a) ^{82}Ge$(n,\gamma)^{83}$Ge and (b) ^{84}Se$(n,\gamma)^{85}$Se. The cross sections are calculated using the density form of the EM operator with (blue, dot-dashed) and without the semidirect (SD) contribution (black, solid) and using the current form of the EM operator with (green, dashed) and without the SD contribution (red, double dot-dashed).

involve orthogonal overlaps of wave functions with the same quantum numbers at different energies. The orthogonality is not complete as the potential for the bound state has been adjusted, relative to the initial state, to reproduce the binding energy. The only other allowed $M1$ transition, of a $d_{3/2}$ neutron captured to the $1d_{5/2}$ bound state, is suppressed by an $\ell = 2$ centrifugal barrier. The $M1$ overlap integral in this case of d-wave capture is three orders of magnitude smaller than the corresponding p-wave $E1$ overlap integral. There is also an additional hindrance factor of $(\hbar c/2M_n c^2)^2 \approx 0.01$ in favor of $E1$ relative to $M1$ transitions [44].

A conventional density form of the EM operator, $e \cdot j_\ell(qr)$, was used, where ℓ is the multipolarity of the EM transition and j_ℓ is the spherical Bessel function of order ℓ. Since the density form of the EM operator is obtained by a (nonrigorous) application of Siegart's theorem [45,46] to a single-particle model [47], a current form of the EM operator, that is, $\vec{j} \cdot \vec{A}$ [35,47], was also considered. The difference between the two cross sections was found to be relatively small, on the order of ≈3%, as seen in Fig. 11. This is encouraging, as it is an indication that the calculation is as consistent as possible in a single-particle model; this is related to the fact that the potential used for the bound states was nearly identical to that used for scattering states [47].

V. SUMMARY

Radioactive ion beams of ^{82}Ge and ^{84}Se were used to study the ^{2}H(^{82}Ge, p)^{83}Ge and ^{2}H(^{84}Se, p)^{85}Se reactions for the first time. The low-lying states of ^{83}Ge and ^{85}Se populated in the (d, p) reactions were studied to reveal their excitation energies, spins, and parities. From proton differential cross sections and systematics of $N = 51$ isotones, the ground and first excited ($E_x = 0.28 \pm 0.02$ MeV) states of ^{83}Ge are determined to have $J^\pi = 5/2^+$ and $J^\pi = 1/2^+$, respectively. The measurement of ^{85}Se confirmed the energies the first three states and the average excitation energy of a doublet consisting of the third and fourth excited states, as determined in a previous study of γ-ray transitions following the β decay of ^{85}As [12]. The spins and parities of the first two states, determined by analyzing the proton differential cross sections, support the tentative assignments of Omtvedt *et al.* [12] of $J^\pi = 5/2^+$ for the ground state and $J^\pi = 1/2^+$ for the first excited state. Level assignments cannot be made for the other states populated in the present measurement.

Spectroscopic factors were extracted for many of the levels populated in this study. However, the measurements are of peripheral reactions, and the usual DWBA analysis of differential cross sections relies on details to which the measurements are insensitive. The spectroscopic factors have significant uncertainties associated with these ambiguities. Asymptotic normalization coefficients that describe the behavior of the tail part of the overlap function, but do not suffer from the same uncertainties as the spectroscopic factors, are also extracted. It is the ANC that can be used reliably across measurements or calculations that are more sensitive to, for example, bound-state potential geometries.

Shell-model calculations were performed in the $N = 51$ region above a core of ^{78}Ni with the shell-model code ANTOINE

[30,31]. The model space is characterized by both a nucleon-nucleon interaction, starting from the Bonn potential model [26] renormalized by building a reaction G matrix, and one of two chosen sets of single-particle energies in the space. The two sets differ in the placement of the proton $0g_{9/2}$ orbital. With both sets, there is qualitative agreement between the calculations and the general trends of the $N = 51$ isotones. The $5/2^+$ state is always the lowest, with the splitting between the $5/2^+$ and $1/2^+$ states generally decreasing from ^{91}Zr to ^{83}Ge. The calculated spectroscopic factors for the $N = 51$ isotones also show a general decrease toward ^{83}Ge, as seen experimentally.

The spectroscopic properties of the low-lying states in ^{83}Ge and ^{85}Se influence the rate of direct neutron capture on these nuclei. Because of the proximity of the $N = 51$ isotones to a closed neutron shell, and particularly because of the low neutron separation energies of ^{83}Ge and ^{85}Se, the direct capture rates to these nuclei are expected to be significant components to the total (n, γ) rates. To this end, direct capture cross section calculations have been performed for the neutron capture to the first two states of both ^{83}Ge and ^{85}Se. Both direct and direct-semidirect calculations were performed, with the results showing that the DSD process via the giant dipole resonance contributes destructively to the overall direct capture cross section. The dominant contribution to the captures comes via the capture of p-wave neutrons with an $E1$ transition to the first two states of both ^{83}Ge and ^{85}Se. Modified spectroscopic factors from those extracted from the (d, p) measurements were used in the summation of the contributions of individual final states in the $N = 51$ nuclei. The spectroscopic factors were modified to ensure that the bound-state wave functions used in the direct capture calculations included the correct asymptotic normalizations, as measured by the ANCs. These modifications were of the order of 5%–15%, within the uncertainties of the spectroscopic factors extracted directly from comparison with DWBA calculations.

ACKNOWLEDGMENTS

The authors would like to thank A. M. Mukhamedzhanov for useful discussions on asymptotic normalization coefficients, M. Hjorth-Jensen for useful discussions and supplying the two-body interaction for the shell-model calculations, and F. S. Dietrich for useful discussions and permission to use the direct-semidirect capture code CUPIDO. KLJ would like to thank the Lindemann Trust. This work was supported in part by the National Science Foundation under Contract No. NSF-PHY-00-098800; the U.S. Department of Energy under Contract Nos. DE-FC03-03NA00143 (Rutgers), DE-AC05-00OR22725 (ORNL), DE-FG02-96-ER40955 (TTU), and DE-FG03-93ER40789 (Mines); and the LDRD program of ORNL.

[1] T. Otsuka, R. Fujimoto, Y. Utsuno, B. A. Brown, M. Honma, and T. Mizusaki, Phys. Rev. Lett. **87**, 082502 (2001).
[2] N. A. Smirnova, A. De Maesschalck, A. Van Dyck, and K. Heyde, Phys. Rev. C **69**, 044306 (2004).
[3] J. Dobaczewski, W. Nazarewicz, T. R. Werner, J. F. Berger, C. R. Chinn, and J. Decharge, Phys. Rev. C **53**, 2809 (1996).
[4] B. Chen, J. Dobaczewski, K.-L. Kratz, K. Langanke, B. Pfeiffer, F.-K. Thielemann, and P. Vogel, Phys. Lett. **B355**, 37 (1995).
[5] C. Freiburghaus, J.-F. Rembges, T. Rauscher, E. Kolbe, F.-K. Thielemann, K.-L. Kratz, B. Pfeiffer, and J. J. Cowen, Astrophys. J. **516**, 381 (1999).
[6] R. Surman and J. Engel, Phys. Rev. C **64**, 035801 (2001).
[7] T. Rauscher, R. Bieber, H. Oberhummer, K.-L. Kratz, J. Dobaczewski, P. Möller, and M. M. Sharma, Phys. Rev. C **57**, 2031 (1998).
[8] J. S. Thomas *et al.*, Phys. Rev. C **71**, 021302(R) (2005).
[9] D. W. Bardayan *et al.*, Phys. Rev. C **63**, 065802 (2001).
[10] http://www.micronsemiconductor.co.uk.
[11] L. A. Montestruque, M. C. Cobian-Rozak, G. Szaloky, J. D. Zumbro, and S. E. Darden, Nucl. Phys. **A305**, 29 (1978).
[12] J. P. Omtvedt, B. Fogelberg, and P. Hoff, Z. Phys. A **339**, 349 (1991).
[13] J. M. Lohr and W. Haeberli, Nucl. Phys. **A232**, 381 (1974).
[14] R. L. Varner, W. J. Thompson, T. L. McAbee, E. J. Ludwig, and T. B. Clegg, Phys. Rep. **201**, 57 (1991).
[15] J. S. Thomas, Ph.D. Thesis, Rutgers University, 2005.
[16] University of Surrey modified version of the code TWOFNR of M. Igarashi, M. Toyama, and N. Kishida (private communication).
[17] C. M. Perey and F. G. Perey, At. Data Nucl. Data Tables **17**, 1 (1976).
[18] M. Bhat, *Evaluated Nuclear Structure Data File* (Springer-Verlag, Berlin, 1992), data extracted using the NNDC Online Data Service from the ENSDF database, file revised as of October 13, 2004.
[19] G. R. Satchler, *Direct Nuclear Reactions* (Oxford University Press, New York, 1983).
[20] J. Rapaport and A. K. Kerman, Nucl. Phys. **A119**, 641 (1968).
[21] J. Rapaport, A. Sperduto, and M. Salomaa, Nucl. Phys. **A197**, 337 (1972).
[22] J. L. C. Ford Jr., K. S. Toth, G. R. Satchler, D. C. Hensley, L. W. Owen, R. M. DeVries, R. M. Gaedke, P. J. Riley, and S. T. Thornton, Phys. Rev. C **10**, 1429 (1974).
[23] H. J. Körner and J. P. Schiffer, Phys. Rev. Lett. **27**, 1457 (1971).
[24] A. M. Mukhamedzhanov, C. A. Gagliardi, and R. E. Tribble, Phys. Rev. C **63**, 024612 (2001).
[25] A. M. Mukhamedzhanov and F. M. Nunes, Phys. Rev. C **72**, 017602 (2005).
[26] R. Machleidt, F. Sammarruca, and Y. Song, Phys. Rev. C **53**, R1483 (1996).
[27] M. Hjorth-Jensen, T. T. S. Kuo, and E. Osnes, Phys. Rep. **261**, 125 (1995).
[28] J. Duflo and A. P. Zuker, Phys. Rev. C **59**, R2347 (1999).
[29] R. R. Whitehead, A. Watt, B. J. Cole, and I. Morrison, *Advances in Nuclear Physics*, edited by M. Baranger and E. Vogt (Plenum, New York, 1977), vol. 9.
[30] E. Caurier and F. Nowacki, Acta Phys. Pol. B **30**, 705 (1999).
[31] E. Caurier, shell-model code ANTOINE, IRES, Strasbourg (1989–2004).

[32] K. Haravu, C. L. Hollas, P. J. Riley, and W. R. Coker, Phys. Rev. C **1**, 938 (1970).
[33] T. P. Cleary, Nucl. Phys. **A301**, 317 (1978).
[34] R. D. Rathmell, P. J. Bjorkholm, and W. Haeberli, Nucl. Phys. **A206**, 459 (1973).
[35] W. E. Parker *et al*., Phys. Rev. C **52**, 252 (1995).
[36] J. Okolowicz *et al*., Phys. Rep. **374**, 271 (2004).
[37] N. Michel, W. Nazarewicz, M. Ploszajczak, and J. Okolowicz, Phys. Rev. C **67**, 054311 (2003).
[38] A. Volya and V. Zelevinsky, Phys. Rev. Lett. **94**, 052501 (2005).
[39] A. J. Koning and J. P. Delaroche, Nucl. Phys. **A713**, 231 (2003).
[40] G. E. Brown, Nucl. Phys. **57**, 339 (1964).
[41] F. S. Dietrich, Phys. Rev. Lett. **38**, 156 (1977).
[42] http://www-nds.iaea.org/RIPL-2/gamma/gdr-parameters-theor.dat.
[43] E. Krausmann, W. Balogh, H. Oberhummer, T. Rauscher, K.-L. Kratz, and W. Ziegart, Phys. Rev. C **53**, 469 (1996).
[44] J. M. Blatt and V. F. Weisskopf, *Theoretical Nuclear Physics* (Wiley, New York, 1952).
[45] A. J. F. Siegart, Phys. Rev. **52**, 787 (1937).
[46] A. DeShalit and H. Feshbach, *Theoretical Nuclear Physics, Volume I: Nuclear Structure* (Wiley, New York, 1974).
[47] J. M. Lafferty and S. R. Cotanch, Nucl. Phys. **A373**, 363 (1982).